

Review

Lev A. Matveev*, Vladimir Y. Zaitsev, Aleksander L. Matveev, Grigory V. Gelikonov, Valentin M. Gelikonov and Alex Vitkin

Novel methods for elasticity characterization using optical coherence tomography: Brief review and future prospects

Neue Verfahren zur Charakterisierung der Elastizität unter Nutzung der optischen Kohärenztomographie: Kurzes Review und Zukunftsaussichten

Abstract: In this paper, a brief overview of several recently proposed approaches to elastographic characterization of biological tissues using optical coherence tomography is presented. A common feature of these “unconventional” approaches is that unlike most others, they do not rely on a two-step process of first reconstructing the particle displacements and then performing its error-prone differentiation in order to determine the local strains. Further, several variants of these new approaches were proposed and demonstrated essentially independently and are based on significantly different principles. Despite the seeming differences, these techniques open up interesting prospects not only for independent usage, but also for combined implementation to provide a multifunctional investigation of elasticity of biological tissues and their rheological properties in a wider sense.

***Corresponding author: Lev A. Matveev**, Institute of Applied Physics RAS, 46 Uljanova Str., Nizhny Novgorod 603950, Russia; Nizhny Novgorod State Medical Academy, 10/1 Minin Square, Nizhny Novgorod 603005, Russia; and Nizhny Novgorod State University, Gagarina Avenue 23, Nizhny Novgorod 603950, Russia, e-mail: lionnn52rus@mail.ru

Vladimir Y. Zaitsev, Grigory V. Gelikonov and Valentin M. Gelikonov: Institute of Applied Physics RAS, 46 Uljanova Str., Nizhny Novgorod 603950, Russia; Nizhny Novgorod State Medical Academy, 10/1 Minin Square, Nizhny Novgorod 603005, Russia; and Nizhny Novgorod State University, Gagarina Avenue 23, Nizhny Novgorod 603950, Russia

Aleksander L. Matveev: Institute of Applied Physics RAS, 46 Uljanova Str., Nizhny Novgorod 603950, Russia; and Nizhny Novgorod State Medical Academy, 10/1 Minin Square, Nizhny Novgorod 603005, Russia

Alex Vitkin: Nizhny Novgorod State Medical Academy, 10/1 Minin Square, Nizhny Novgorod 603005, Russia; and Department of Medical Biophysics, University of Toronto, 610 University Ave., Toronto, Ontario M5G 2M9, Canada

Keywords: optical coherence tomography; optical elastography; tissue mechanical properties characterization; speckle decorrelation; tissue relaxation rate; optical palpation.

Zusammenfassung: In diesem Beitrag wird ein kurzer Überblick über einige kürzlich vorgestellte Ansätze zur elastographischen Charakterisierung von biologischen Geweben mittels optischer Kohärenztomographie gegeben. Diesen “unkonventionellen” Ansätzen ist gemeinsam, dass sie nicht, so wie die meisten anderen, auf einem zweistufigen Prozess (zuerst Rekonstruktion der Partikelverschiebungen, dann Durchführung ihrer fehleranfälligen Differenzierung), basieren, um die lokalen Belastungen zu bestimmen. Es wurden mehrere Varianten dieser neuen Ansätze verfolgt, die auf deutlich unterschiedlichen Prinzipien beruhen und im Wesentlichen unabhängig voneinander demonstriert wurden. Trotz der scheinbaren Unterschiede, eröffnen diese Techniken interessante Perspektiven – nicht nur für eine unabhängige Nutzung sondern auch für die kombinierte Umsetzung – um eine multifunktionale Untersuchung der Elastizität von biologischen Geweben und ihrer rheologischen Eigenschaften in einem weiteren Sinne zu ermöglichen.

Schlüsselwörter: optische Kohärenztomographie; optische Elastographie; Charakterisierung der mechanischen Gewebeeigenschaften; Speckle-Dekorrelation; Gewebere-laxationsrate; optische Abtastung.

DOI 10.1515/plm-2014-0023

Received June 14, 2014; revised August 6, 2014; accepted August 8, 2014; previously published online September 3, 2014

1 Introduction

A common indication of pathological processes in a biological tissue is the change in its mechanical (or in a wider sense – rheological) properties. It is well known, for example, that cancerous tumors are usually stiffer than their surroundings [1]. In the last two decades, various elastographic techniques were developed to focus on this pathological property for early cancer diagnosis/detection, with the goal of possibly reducing invasive biopsy procedures [2, 3]. To detect the changes of tissue mechanical properties at the earliest stages, it is necessary to increase the resolution and sensitivity of elastographic examination. For this purpose, the elastography based on optical techniques such as optical coherence tomography (OCT) has been developed over the last 15 years, the seminal paper by Schmitt [4] being one of the first publications on this topic. In comparison with other elastographic techniques developed in medical ultrasound (US) or magnetic resonance imaging, the OCT-based elastography (optical coherence elastography, OCE) ensures significantly higher resolution, potentially enabling better localization and earlier detection of pathological regions [5–17].

Several review papers were published in recent years on the progress in the field of OCE [18–20]. As seen from these reviews, despite the great interest in the implementation of the elastographic regime in OCT and numerous demonstrations, OCT devices with an elastographic mode are not yet commercially available for clinical applications and routine examinations of patients. In contrast, there are some US elastographic techniques that are already implemented on several multi-modal and specialized-for-elastography commercial platforms [2, 3]. Thus, so far the successfully tested OCE techniques are more individualized, focused on specific problems and diseases, and are mainly used in assessing rather specific cases for which they are adopted.

There is a group of recently developed OCE methods based on OCT-based direct observation of propagation of shear (or surface) elastic waves in order to evaluate the shear elastic modulus that determines the propagation velocity of these waves (e.g., [21–31]). Consequently, such techniques require additional devices for excitation of the shear/surface waves, which (in comparison with compression OCE where the OCT probe itself is used for producing compression) complicates the construction of OCT systems and correspondingly limits the practical application areas of such techniques, particularly for endoscopic examinations.

Another “traditional” group of OCE methods can be termed as “displacement-based (DB) approaches” (usually

earlier developed quasistatic compression techniques [5, 6]). These require initial reconstruction of the displacement field in the inspected tissue subjected to quasistatic deformation that can often be produced by the rigid surface of the OCT probe itself. Particular implementations of the displacement-field reconstruction can be rather different and are often based on ideas transferred from US. Among these, correlational tracking of speckles in intensity OCT images has been widely studied since the appearance of Schmitt’s paper [4]. Other modifications of this processing approach based on the use of full-field data have been proposed [13]. However, such approaches to OCE have not yet moved beyond laboratory tests and experimental validations have been mostly performed using phantoms. The main impediment in the further development of such techniques lies in the high sensitivity of these methods to different types of artifacts, such as speckle blinking and boiling in images of deformed tissues and other OCT signal features arising during *in vivo* inspections. Many of these difficulties relate to motion artifacts [10, 31–33] and speckle decorrelation [34–38], reducing the robustness of such OCE techniques.

To overcome the complications inherent in correlational tracking of particle displacements, phase-sensitive methods (see, e.g., [8] and recent modifications [39]) for measuring particles’ displacements are actively studied in recent years as a promising alternative to correlational tracking, which intrinsically ensures much better robustness with respect to speckle blinking effects [40]. However, the phase-sensitive OCE, despite its higher sensitivity (down to nano- and even picometer displacements) actually ensures the same precision of initial localization of the scatterers as in the initial OCT images. This precision is limited by the OCT system resolution, the typical value being on the order of 5–20 μm and thus is orders of magnitude lower than the displacement sensitivity of phase-sensitive methods. Further, to obtain local strains in the inspected region, the phase methods also require performing error-sensitive differentiation. The accuracy of the latter depends not only on the accuracy of measuring displacements of the scatterers, but also on the accuracy of determining their initial positions. Consequently, analogous problems as encountered by the correlation-tracking techniques to a significant degree remain in phase OCE methods. In view of these difficulties common to all DB approaches, OCE methods that do not rely on the initial reconstruction of the displacement field may be preferable.

In this paper several of such recently proposed “unconventional” OCE techniques are reviewed, with interesting prospects for implementation of elastographic

mode in OCT. While each of these methods comes with its set of advantages and drawbacks, their overall principles suggest new solutions for solving the problem of insufficient robustness of traditional (displacement-field-reconstruction based) elastographic approaches. One may expect these techniques to be implemented in emerging multimodal OCT devices, to further extend the useful information content afforded by OCT assessment of biological tissue.

2 Novel approaches to OCE

In this section, several recently proposed “unconventional” OCE approaches are considered. These were proposed and demonstrated essentially independently; however, despite their apparent differences, they suggest interesting possibilities for their combined implementation based on quite conventional OCT devices. This should enable multifunctional investigation of elasticity of biological tissues (and their rheological properties in a wider sense), as discussed in the end of this section.

2.1 Stiffness characterization based on tissue relaxation rate

The approach to OCE based on the tissue relaxation rate measurements was considered in [41]. The main idea is to observe the process of the shape recovery of the tissue surface deformed by an impact. The deformation was achieved using an air-pulse system with a ~ 1 ms pulse duration, resulting in the tissue displacement on the order of several micrometers. Then the displacement of the tissue surface was measured using phase-sensitive OCT and the time dependence of displacement fitted by an exponential function to extract the relaxation rate. The authors showed that the relaxation rate was weakly dependent on the impact force (i.e., pressure in the air-pulse system and the distance between its nozzle and the tissue). Such robustness with respect to the perturbing-impact parameters is an attractive feature of this approach (Figure 1A). The relaxation constant for gelatin phantoms was shown to vary approximately linearly with gelatin concentration (Figure 1B). This is in agreement with a previous publication of the same authors [42] showing that the stiffness of the gelatin phantoms also varies nearly linear with the amount of gelatin (Figure 1C). For characterization the stiffness of soft biological tissues, either the Young modulus E that describes the material reaction to

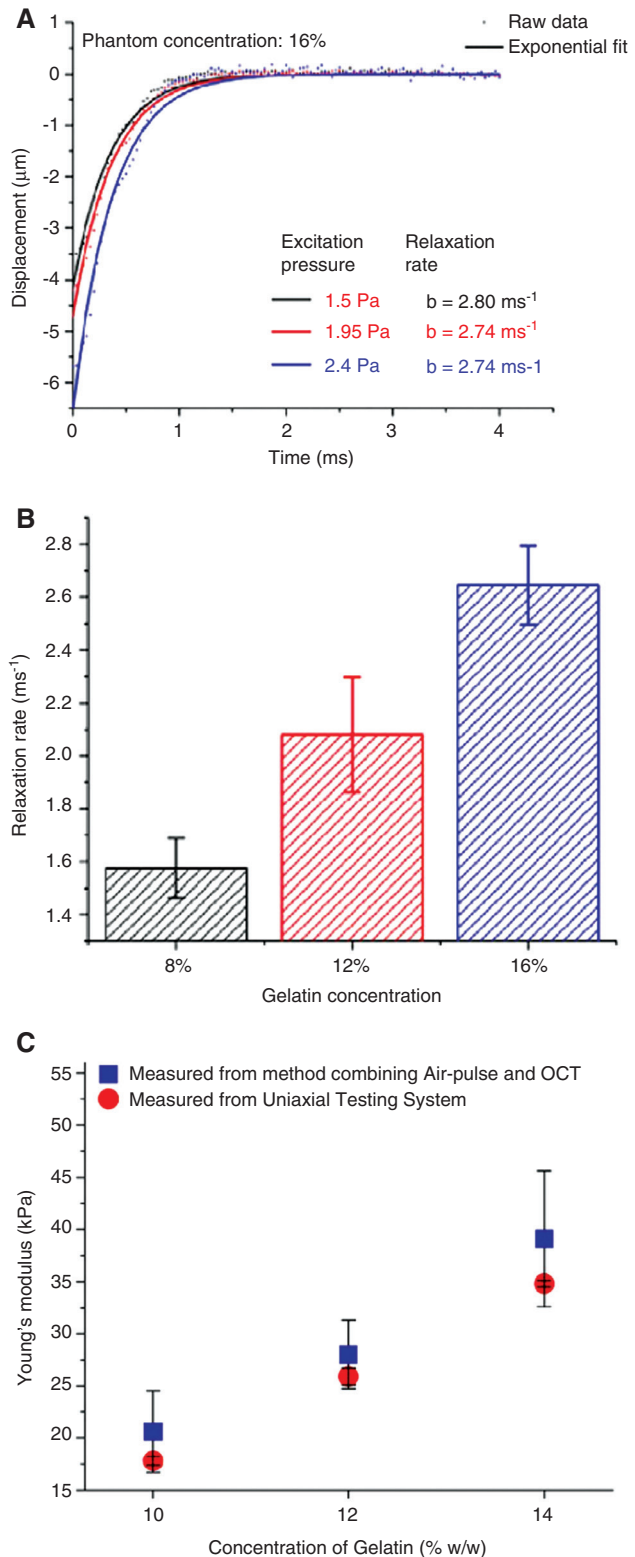


Figure 1 (A) Relaxation process in the gelatin under different excitation pressures of an air-puff impulse, (B) dependence of the fitting parameter on gelatin concentration, and (C) dependence of gelatin Young's modulus on its concentration. Panels (A) and (B) reprinted from [41] and panel (C) reprinted from [42] with permission.

uniaxial stress, or the shear modulus G that corresponds to the material reaction to shear stress one be equivalently used. The reason for this near-equivalence is that for soft tissues, the Poisson's ratio ν is very close to 0.5, so that the well-known general relation between these moduli, $E=2(1+\nu)G$, with a high accuracy reduces to the simple proportionality $E\approx 3G$ for all soft biological tissues. Bearing in mind this remark, the results of [41, 42] indicate that the observed differences in relaxation rate (which is a rheological viscoelastic parameter) is mostly determined by the variations in the sample tissue elasticity. In addition to phantom studies, this approach was tested pre-clinically *in vivo* for assessment of age-related changes in mouse cornea [41].

These results are encouraging for eventual clinical implementation, specifically due to relative independence of this variant of OCE to the details of impact parameters. Such robustness is important as these deformations are difficult to apply in a controlled and reproducible fashion. It is also clear that even though the surface deformation is measured at “one point”, the measured data are averaged not only over the cross section of the optical beam and a certain depth of the light penetration into the tissue depth, but in fact the averaging is made over the entire volume of the tissue mechanically involved into the relaxation process. The characteristic size of this region of effective averaging is not evident, but is likely on the order of the lateral size of the displaced surface in all dimensions, (i.e., ~several hundred micrometers). This averaging can be considered as a positive feature further adding to the robustness of the technique; however, this “one-point” (although averaged) approach presents a challenge of constructing two-dimensional (2D) or three-dimensional (3D) relaxation rate maps. Apparently this problem may be solved by changing the scanning patterns, for example performing a series of B-scans, which in turn would require sufficiently high acquisition rates, because the characteristic relaxation times can be on the order of a few milliseconds [41]. The latter value exceeds the typical acquisition period of obtaining A-scans for many systems, but is significantly smaller than the typical acquisition rate of B-scans.

2.2 OCT-based palpation using a compliant “control” sensor

An interesting approach to OCE combining classical palpation and OCT imaging was recently proposed in [43] under the name of “optical palpation”, clearly reflecting the method's principle. It is based on the visualization

of deformation of an intermediate translucent compliant layer with previously measured properties placed between the rigid surface of the OCT probe and the inspected tissue. The intermediate layer plays the role of a compliant sensor, because the dependence of its thickness on the applied stress can be calibrated prior to the measurements. The thickness of the intermediate layer can be in the sub-mm range. A key point is that when the OCT probe (a few mm in diameter) is pressed to the surface of a homogeneous tissue like a piston, an approximately uniform stress field should be created in the probe vicinity within the depth of the order of the probe diameter. However, if a stiffer inclusion is located within this zone, its weaker deformability results in higher straining of the softer layers located above the inclusion. Consequently, if below the OCT probe a uniform compliant layer is placed, the variation in the thickness of this layer is larger above tissue regions containing a buried stiff inclusion. These variations in the intermediate layer thickness can be readily visualized at the OCT image (Figure 2A–F) even if at the depth of the stiffer inclusion location, the OCT signal is too weak (i.e., insufficient to visualize the inhomogeneous displacement field around the inclusion). Therefore, the depth where the stiffer region can be detected via the “mechanical imprint” in the form of inhomogeneous deformation of the compliant sensor can be significantly (several times) greater than the zone directly visualized in the OCT image. This increased sensing depth of the optical palpation approach [43] is a very attractive feature of this technique.

This OCE approach is robust, in that the compliant sensor layer can be preliminary calibrated, which makes this technique less sensitive to optical and other artefacts of underlying tissue including strain-induced speckle decorrelation and motion noise. In fact the results' accuracy is mostly determined by the robustness of the OCT imaging of the compliant sensing layer with controllable (or at least preliminary calibrated) properties. This largely eliminates the necessity of fine tuning the whole OCE system for each individual investigation, as typical of many other OCE approaches. In particular, as demonstrated in [43], the described optical palpation provides the opportunity to characterize the elasticity distribution in transparent (without any scatterers) or opaque tissues that cannot be directly visualized in the conventional OCT images.

However, the fact that such measurements are performed only within the compliant sensing layer underscores the principal complexity of visualizing the depth-distribution of the stiffness. Despite the difficulty of depth-resolved elasticity mapping, the strength of the

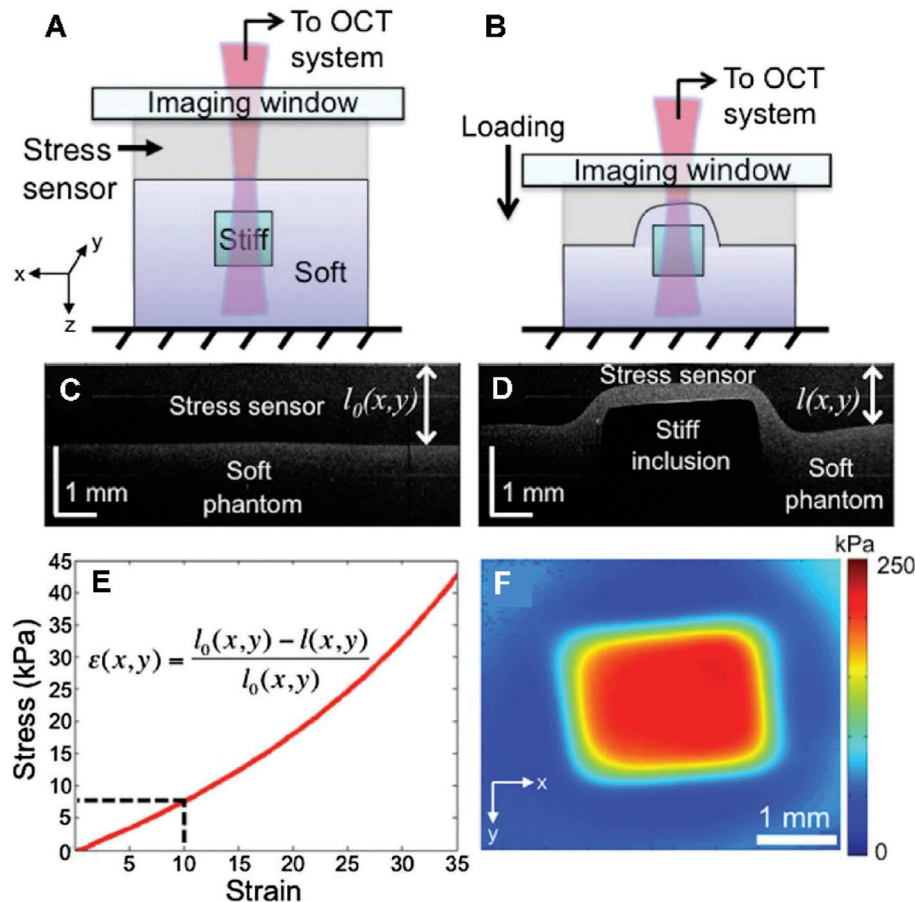


Figure 2 Principle of the “optical palpation” approach. (A) Initial state of the sensor and tissue. (B) The stiffer region causes larger strain in the corresponding sensor region. (C and D) OCT images of the situations mentioned in (A) and (B). (E) Calibration results of the stress-strain dependence for the sensor and (F) *en-face* elastogram. Reprinted from [43] with permission.

proposed OCE palpation is that it already provides robust 2-D *en-face* elasticity maps. Although including the depth dimension for a full 3-D elasticity map is yet to be demonstrated, 2-D *en-face* elastography has indeed been shown in phantoms and in freshly excised human breast tissue from a female breast cancer patient undergoing mastectomy [43].

Since the stress-strain dependence for the layer sensor can be calibrated (Figure 2E), not only qualitative, but also quantitative stress distribution in the *en-face* projection can be obtained under the sensor (Figure 2F).

In the context of the calibration of the sensing layer properties, noticeable nonlinearity of the strain-stress relation can be seen in Figure 2E. This deviation from the linear Hooke’s law dependence is also reported for many soft biological tissues and is often the consequence of the geometry of the observation conditions rather than real nonlinearity of the material properties. In fact, proper definition of Young’s modulus corresponds to perfectly

uniaxial stress in the measured sample. This requirement is usually satisfied for elongated rod-like samples with free lateral boundaries subjected to elongation or compression in the axial direction. In this case small areas near the rod ends that are usually clamped or glued to the measurement system do not produce significant contribution to the stress-strain behavior of the sample. Conversely, a layer compressed between two solid surfaces represents a much different situation, especially if its thickness is smaller than its lateral dimensions. Since soft biological tissues are “rubber-like” (i.e., have the Poisson’s ratio close to 0.5, similar to liquids), the decrease in the layer volume due to its axial squeezing should be almost exactly compensated by the tissue expansion in the lateral direction. However, in contrast to liquids, the elastic tissue layer has a finite shear modulus. Further, its upper and lower boundaries cannot move freely, but are “stuck” to contacting boundaries. Consequently, the developed near-boundary tangential forces impede lateral

displacements of the layer and do not allow for free compensation of the decrease in the layer volume. In the areas close to the layer center, the tissue particles almost do not displace in the lateral direction, so that the character of the rubber-like tissue deformation resembles the conditions of hydrostatic compression. The latter is controlled by the bulk modulus of the material that is much greater than the Young's modulus. In view of this, during squeezing rubber-like tissue between two solid surfaces without sliding, the apparent Young's modulus initially may be close to the genuine Young's modulus, whereas for very strong squeezing the observed compressibility is dictated by the bulk modulus that is orders of magnitude greater. This transition looks as apparent strong nonlinearity of the material even if the tissue may actually obey the linear Hooke's law.

Certainly, the importance of this measurement artifact depends on the ratio between the initial thickness of the layer and its size in the lateral direction. Correspondingly, the calibration curves shown in Figure 2E are strongly dependent on the specific calibration measurement conditions. Furthermore, the calibration procedure implies that the control layer is squeezed between two rigid boundaries, whereas in the measurements described in [43], only the upper layer boundary is "stuck" to the rigid surface of the OCT probe, whereas the bottom contacts the inspected soft tissue. Under such boundary conditions, the character of layer expansion is not that strong restricted as for the rigid boundary at the bottom, and the apparent nonlinearity of the layer is not that pronounced. Nevertheless, this effect can be quite noticeable. For example, in the experiments with two-layer silicone phantoms described in [34], the apparent relative softness of the upper softer layer noticeably decreased from over 3 times to about 2 times under increased compression by the OCT probe when the thickness of this layer decreased from about 350 μm –100 μm . The probe diameter was 2 mm. Therefore, quantification of the tissue stiffness and its Hooke's law behavior under increasing compression should account for apparent nonlinearity that is likely caused by the measurement conditions. Lubrication of the contact between the solid surface of the probe and the tissue can hardly ensure "free" expansion of the tissue in the lateral direction, because the characteristic time of such expansion usually should be much greater than the typical interval between the compared images (on the order of 5–50 ms for B-scans and even less than a millisecond for A-scans used in phase-sensitive techniques).

More detailed discussion of these issues is beyond the scope of this review, although from the viewpoint of quantification this is an important feature for the described

approach. Overall, the optical palpation method proposed in [43] looks as a rather interesting alternative to the conventionally discussed DB approaches, in view of the key role of the highly controllable translucent layer and consequent intrinsic robustness to various OCT signal artifacts and instabilities typical of OCT images of real biological tissues.

In the next section, another unconventional OCE technique that also does not require initial displacement-field reconstruction, the so-called correlation-stability (CS) approach [34, 44] is described. Moreover, the possibilities for combining the optical palpation method [43], the relaxation approach [41], and the CS approach are briefly discussed.

2.3 Correlation-stability approach and its speckle variance modification OCE

It is well known that numerical differentiation (either directly via finite differences or using equivalent indirect methods) is a rather error-sensitive procedure [40]. The necessity of this error-sensitive procedure is common for any variant of "conventional" approaches based on the initial reconstruction of the displacement field (including various types of correlational speckle tracking, as well as phase methods). Therefore, a method that would skip this error-prone step to directly extract information on the local tissue strains would be a welcome addition to the field.

An attractive alternative OCE approach, in which the intermediate error-sensitive stages of the displacement-field reconstruction and its subsequent differentiation are avoided, is based on correlation stability of OCT images of deformed biological tissues [34, 44–47]. Generically, it also uses the main idea of the compressional elastography, i.e., the fact that under the same stress, the degree of tissue deformation depends on its local stiffness. Consequently, for stiffer regions, the similarity between the pre- and post-compression OCT images is higher, and thus the maximum zero mean normalized cross-correlation function (ZMNCC) should also be higher. Therefore, suitably computed cross-correlation maps of compressed tissues should yield the spatial distribution of relative stiffness. In general, this idea is close to correlation-mapping OCT utilized for micro-vasculature visualization, where the speckle decorrelation is produced by the Brownian motion of scatterers in liquids [48–51]. However, in contrast to such correlation mapping, for the elastographic use of the CS approach, tissue deformation must be applied.

Cross-correlation in the elastographic CS approach should be performed using a sliding window in order to compensate the decorrelation of the compared images due to trivial translational motion of the scatterers in the deformed sample, thus retaining only the strain-induced decorrelation of interest [34, 44, 52]. This compensation should be made with a sufficiently high sub-pixel accuracy, which is possible via processing full complex signal (complex amplitude) OCT signals [52, 53]. The robustness of this approach is afforded by its lower sensitivity to the average error in determination of the displacement field over the entire image, in contrast with the DB approaches. In the latter, the decorrelation related to the strain-induced speckle blinking/boiling is a negative factor: if the correlation drops significantly in the soft part of the tissue, the error of the displacement field reconstruction inside this part of the tissue increases accordingly. In the CS elastographic mapping, this strong decorrelation hinders accurate strain field reconstruction inside this soft part of the tissue as well, but nevertheless permits to map the region of increased strain directly via significant reduction of cross-correlation [34, 44, 45].

In general, the above ideas remain the same for image features at different scales, but there are significant differences between mechanisms of cross-correlation reduction either due to purely geometrical distortions [44] or due to the strain-induced intensity variations (the so-called speckle blinking/boiling) in the speckle patterns formed by scattered fields from sub-resolution scatterers [34]. Moreover, in some cases the transition from one case to another can be made by changing the OCT system parameters. For example, strain-induced speckle intensity-variation rate can be decreased by lowering the ratio of the OCT source wavelength and its coherent length [34, 40, 45].

For most of the conventional OCT devices used for inspection of real biological tissues or similar phantoms, the regime of speckle decorrelation is often realized [34]. Moreover, speckle decorrelation during the speckle “blinking” usually occurs earlier than the decorrelation induced by any of purely geometrical distortion (translations and geometrical deformations) of speckle patterns [34, 40, 45]. Consequently, reconstruction of displacements via speckle-tracking is significantly complicated because of high strain-induced speckle decorrelation rate [40]. Despite this, the CS approach allows to visualize the distribution of local strains inside the medium. Figure 3 illustrates CS-derived qualitative elasticity characterization of a two-layer silicone phantom displaying a real OCT image of the phantom (Figure 3A) and the corresponding CS elastography map (Figure 3B). The sample is a two-layer phantom made of silicone with the stiffness contrast between the layers of $\sim 3\times$. As seen, the stiffer layer is well visualized via its higher correlation stability.

In its simplest implementation, the CS approach provides only qualitative mapping of the stiffness in the inspected region with a spatial resolution determined by the size of the used correlation window. Quantitative characterization of elasticity distribution using the CS approach is challenging. Recently, an advanced CS variant was proposed to address the quantification of the stiffness differences [53, 54]. This modification of the CS approach is somewhat similar to speckle-variance due to the Brownian motion in the micro-vasculature visualization [55–60]. Instead of ZMNCC, a closely related normalized speckle intensity variation function (NSIVF) can be used. NSIVF for two subsets (initial and deformed states) is given by:

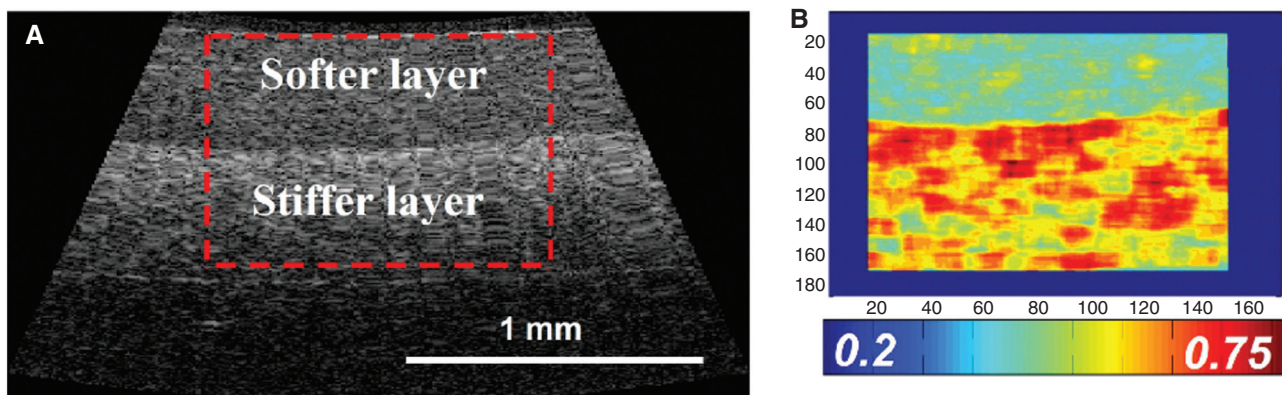


Figure 3 Example of a structural OCT image of a two-layer silicone phantom (A) and the resulting correlation-stability map of relative stiffness (B) obtained via speckle-level correlation processing. Under compression, the upper softer layer experiences stronger deformation and thus is stronger decorrelated compared with the stiffer underlying layer. Color-bar is the value of ZMNCC and units of the axis are pixels. Reprinted from our previous publication [34].

$$V = \frac{\text{Var}(|S|^2 - |F_{n^*,k^*}|^2)}{\text{Var}(|S|^2) + \text{Var}(|F_{n^*,k^*}|^2)}, \quad (1)$$

where

$$\text{Var}(|\bullet|^2) = \frac{1}{m_1 m_2} \sum_{i=1}^{m_1} \sum_{j=1}^{m_2} (|\bullet|^2 - \text{mean}(|\bullet|^2))^2, \quad (2)$$

and S and F_{n^*,k^*} are the subsets (with a full complex signal OCT quadratures amplitude signal recorded as complex number for each pixel) $m_1 \times m_2$ in size taken from the initial and deformed images, the quantities (n^*, k^*) correspond to the vector of translational displacement of the subset F_{n^*,k^*} with respect to S . Here, $\text{mean}[\cdot]$ is the mean value of intensity of the respective subsets taken from the reference and deformed frames. It can be shown [40, 54] that for moderate strains, NSIVF is related to the strain ε as $\sqrt{V} \propto \varepsilon$. This means that for the local strains $\varepsilon_{1,2}$ determined by the elastic moduli $E_{1,2}$ of two different regions of the tissue subjected to the same stress in the vicinity of the OCT probe, the following relation is valid [54]:

$$\frac{\sqrt{V_{\text{region1}}}}{\sqrt{V_{\text{region2}}}} = \frac{\varepsilon_1}{\varepsilon_2} = \frac{E_2}{E_1}. \quad (3)$$

Thus this speckle variance-like modification of the CS approach provides the quantification of the stiffness relations in different regions. The ZMNCC is related to NSIVF as:

$$V = 1 - 2 \cdot C(n^*, k^*) \cdot \frac{\sqrt{\text{Var}(|S|^2) \cdot \text{Var}(|F_{n^*,k^*}|^2)}}{\text{Var}(|S|^2) + \text{Var}(|F_{n^*,k^*}|^2)}, \quad (4)$$

where

$$C(n^*, k^*) = \frac{\frac{1}{m_1 m_2} \sum_{i=1}^{m_1} \sum_{j=1}^{m_2} \{(|S_{i,j}|^2 - \text{mean}(|S_{i,j}|^2)) \cdot (|F_{i+n^*,j+k^*}|^2 - \text{mean}(|F_{i+n^*,j+k^*}|^2))\}}{\sqrt{\text{Var}(|S|^2) \cdot \text{Var}(|F_{n^*,k^*}|^2)}} \quad (5)$$

is ZMNCC itself.

As mentioned in [52], speckle intensity variation can be produced by both the translational displacements (related to the speckle translation as a whole and therefore the flux of the intensity from one pixel to another with total luminance energy conservation), as well as by local strains (responsible for speckle blinking without any intensity flux from one pixel to another) [40]. Therefore it is very important to compensate all translational displacements even on sub-pixel level for subset F_{n^*,k^*} relative to reference subset S , so as to retain only the strain-induced contributions to decorrelation and NSIVF

value [53]. The compensation of the translational displacements is based on precise localization of maxima of the absolute value of the complex cross-correlation function for the deformed and reference images by applying small (within ± 0.5 pixel) relative displacements of the compared subsets. Because of discrete nature of the OCT images in the space domain, the Fourier transform of the considered sliding window (subset) into spectral domain was used to perform its displacement with a sub-pixel accuracy. This procedure consists of applying the multiplication of the Fourier-components by the appropriate complex exponential factors in order to obtain the spectrum corresponding to the subset shifted by any desired sub-pixel value in the space domain. Performing the inverse transform, the spatial form of the shifted subset can be obtained and used for calculating the cross-correlation with the reference subset. Iterative maximization of the ZMNCC between the reference and so-shifted subset from the deformed image makes it possible to estimate the displacement of the chosen image fragment with a sub-pixel accuracy and does not require any special assumptions about the form of the cross-correlation function. As a result of such processing, the two subsets taken from the compared images can be superposed with a high sub-pixel accuracy. The uncompensated decorrelation remaining after this process is related to the straining of the subset. After performing such operations, the sought-after quantity NSIVF given by Eqn. (1) for each subset F_{n^*,k^*} from the deformed frame and the subset S from the reference image can be found. The so-calculated value of NSIVF is determined only by speckle blinking induced by local strains, with the contribution of the translational displacements thus excluded.

To demonstrate this idea, OCT images of a three-layer tissue sample have been numerically simulated. This simulation is based on the principle of A-scan formation in full complex signal (complex signal) spectral-domain OCT (FF-SD-OCT), as described in detail previously [61]. In the simulation discussed here, initially 10,000 randomly and uniformly distributed independent scatterers were put in each A-scan which has 2048 μm in depth corresponding to 256 pixels. The depth coordinates of each scatterer were defined with double precision in units of μm (i.e., with a high sub-pixel accuracy). Each B-scan consists of 256 A-scans (so it has 256 \times 256 pixels corresponding to

2×2 mm). The first simulated frame is the reference frame and the others (deformed frames) simulate the tissue straining from 0 up to 3% average (mean values applied to whole sample) strain with a step of 0.1%. During the straining process simulation, the displacement of each scatterer was calculated independently and then the new contributions to the A-scan spectrum were calculated (note that random distribution of the scatterers was generated only once for the reference image and then the strain-induced speckle-pattern evolution was calculated deterministically). In this simulation, the stiffness contrast of the middle layer is 3× of the surrounding softer tissue (as for the silicone phantom described above and illustrated in Figure 3). The ratio of the coherence length L_c to wavelength λ in this simulation is $L_c/\lambda=6$, so that the speckle blinking is fairly noticeable. Applying the above described speckle-variance approach (including the algorithm of sub-pixel compensation of the displacements), one can obtain the strain dependence of \sqrt{V} for both stiffer ($\sqrt{V_{stiff}}$) and softer ($\sqrt{V_{soft}}$) regions.

Figure 4A demonstrates the linear dependence of the square root of NSIVF for stiffer region for strains larger than 0.7%. For strains smaller than 0.7%, the deviation from the linear law is caused by the insufficient

translational displacement compensation for such small displacements (defined by a predetermined threshold error in sub-pixel compensation algorithm). The linear dependency for softer regions is in the strain range from ~0.1% up to 1.4%. For strains exceeding 1.4%, the variance in the softer regions exhibits saturation due to the significantly decorrelated speckle structure. The slopes of the variance curves in the regions of linear behavior exhibit ~3× difference, as is expected from the analytical considerations. As it can be seen from Figure 4B, the ratio $\sqrt{V_{soft}} / \sqrt{V_{stiff}}$ is close to 3 in the strain range from 0.7% up to 1.4%. Figure 4C demonstrates the elastogram plotted on the basis of this speckle-variance OCE approach.

The speckle-variance OCE modification of CS approach allows for quantification of the strain ratios in different regions of the tissue using fast enough FF-SD-OCT devices which ensure sufficiently detailed dependence of the NSIVF on the strain, in order to single out the region of a linear dependence of square roots of NSIVF for different regions of the investigated object. For example, such a correlation (or variance)-based calibration procedure can be performed for the compliant sensor used in the optical palpation method described above.

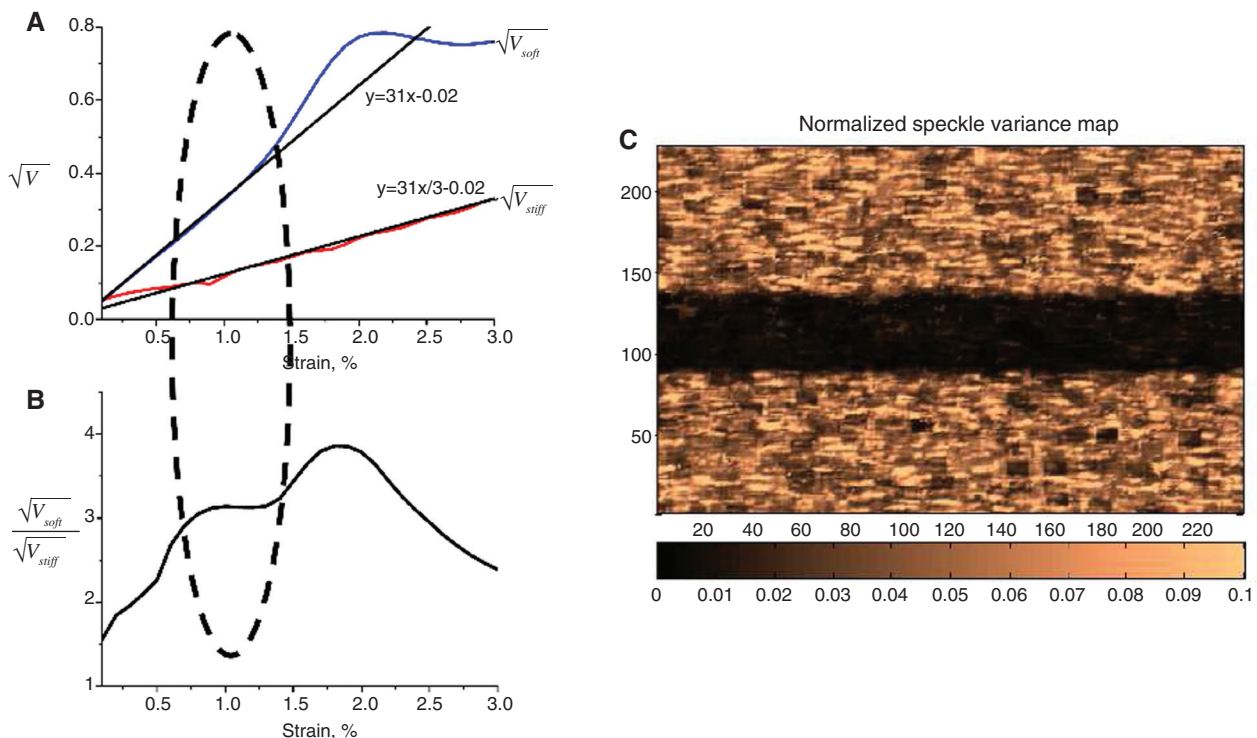


Figure 4 (A) Strain dependence of square root of NSIVF for the stiffer (red curve) and softer (blue curve) regions of a numerically simulated three-layer tissue. The black lines are the fits of its linear parts, where the slope ratio corresponds to the stiffness ratio. (B) Region where this ratio can be measured, and (C) speckle-variance elastogram under strain 1%. Color-bar is the value of NSIVF and units of the axis of (C) are pixels.

Before moving on to the next topic, it is important to note that the CS approach can be applied in two ways: 1) with a single chosen reference frame or other frames, and 2) by cross-correlating each analyzed frame with another one acquiring several steps before or after (the so-called time-sliding reference frame). In the first case, the reference frame is selected only once and then the CS processing is applied to the entire sequence of subsequent frames. It means that the time delay between reference and each subsequent analyzed frames increases monotonically. One can choose, for example, the first frame from a sequence as the reference one and then cross-correlate all other frames with it (second with first, third with first, etc). This process can be used, for example, to obtain the optimal time lag or to analyze some time-dependent (e.g., relaxation) processes. Alternatively, one can fix the time delay between the reference and analyzed frames. This means that for each pair of the processed frames, the time lag is always the same (e.g., suppose the chosen time delay is 3 inter-frame spacings; one would then cross-correlate 4th frame with 1st, 5th with 2nd, etc.). This processing can be used as for obtaining the relaxation rate and for observing periodic natural motions in the tissue (as described below).

2.4 *In vivo* observation of elastographic maps generated by natural periodic tissue motions using OCE based on CS approach

Most of the motion artifacts in biomedical OCT (and OCE) arise from natural motions of either investigator or investigated organism [31, 33]. Here, an example is presented how the natural motions of living tissue can be detected/used for elastographic mapping using the CS approach, specifically to single out the areas where the natural motions produce stronger or weaker decorrelations. The above described CS approach is applied with a time-sliding reference frame to calculate correlation field for each two sequentially obtained frames (meaning a fixed time lag between reference and analyzed frames, equal to twice the inter-frame interval). The correlation-window (subset) size is 3×3 pixels. The frame rate of the used home-made SD-OCT device is 5.25 Hz. The scans contained full complex signal information (based on complex signal) and in the considered example B-scans were 512×256 pixels in size (covering about 3 mm in the horizontal direction and about 1.5 mm depth in air).

The time-sliding correlational processing was applied *in vivo* on a mouse with a hind leg tumor to

determine tissue regions that are most (and least) affected by mouse natural motions. Figure 5A demonstrates the time-evolution correlation field between each pair of adjacent frames (averaged over entire frame). As seen, the correlation between adjacent frames changes significantly. The Fourier transform of the so-obtained signal provides the information about the frequencies of the components arising due to generation of spectral components corresponding to combinations of the OCT device frame rate of 5.25 Hz and periodic mouse movements (Figure 5B). It was found that these mouse motions corresponded to the breathing rate. The analysis of the main peaks in the obtained spectrum shows that the largest peak at 1.56 Hz in the spectrum appeared via the combination of the frame rate with the breathing frequency that can thus be estimated as $5.25 \text{ Hz} - 1.56 \text{ Hz} = 3.69 \text{ Hz}$. The next strong peak corresponds to the combination of double frequency of breathing with the frame rate $2 \times 3.69 \text{ Hz} - 5.25 \text{ Hz} = 2.13 \text{ Hz}$, whereas the smaller third, but still fairly well visible peak corresponds to the difference between the third harmonic of the breathing frequency and the second harmonic of the frame rate $3 \times 3.69 \text{ Hz} - 2 \times 5.25 \text{ Hz} = 0.57 \text{ Hz}$. Figure 5C demonstrates the averaged CS map for the images with the mean correlation larger than 0.4. The correspondence of the clearly seen regions that show different levels of perturbation by the same natural motion (breathing) and histological tissue features in the investigated regions is interesting and will be pursued in the near future. Similar verification of tissue stability before conducting OCE using externally produced compression or applying speckle-variance methods [55–60] or correlation mapping [48–51] for micro-vasculature visualization, may prove useful (as sufficient stability of investigated region is critically important for success of these techniques). In the discussed case, the breathing motion of an anesthetized mouse produced significant instability in the investigated area, which may be addressed by better animal imaging procedures (the type of anesthetic, mouse position on the OCT imager, etc.).

The above-described procedure provides information about the spatial distribution of the strains induced by natural biologic motions, thus enabling a useful “baseline” elastogram. While interesting in its own right, this may also prove useful for preliminary evaluation of the overall stability of the inspected tissue region (thus guiding the necessary measures for stabilization) prior to proper OCE or microvascular OCT imaging. Similar measures may be useful for some other applications, as discussed in the next section.

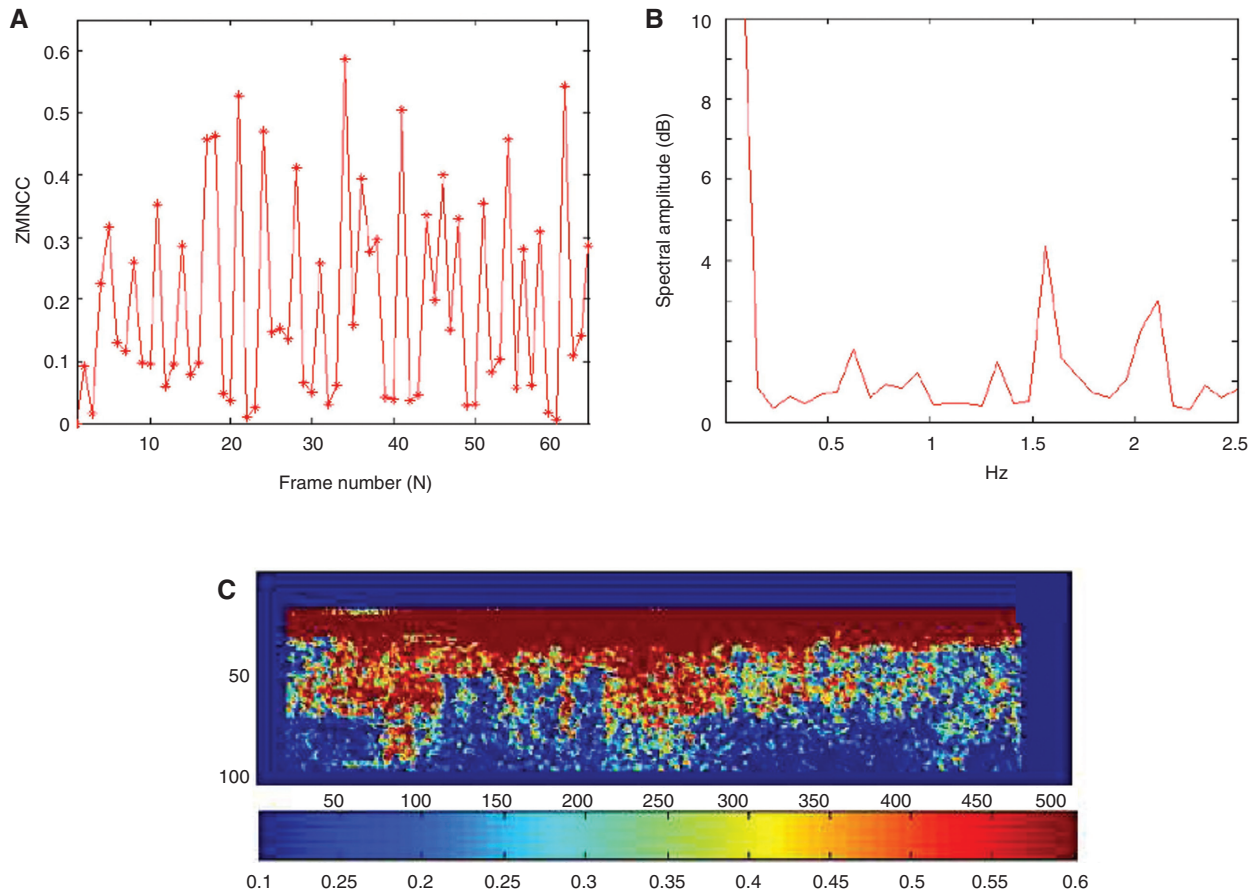


Figure 5 (A) Dependence of the ZMNCC between the two adjacent frames (N and $N-1$) on the frame number N . (B) Fourier transform where the breathing harmonics are visible. (C) Averaged correlation-stability map for the frames with mean (over the entire frame) correlation > 0.4 . Color-bar is the value of ZMNCC and units of the axis of (C) are pixels.

2.5 Possibility of applying the CS approach for studying the tissue relaxation rates and combining with optical palpation

If natural tissue motions in the inspected region are sufficiently reduced, it becomes possible to apply the CS approach, for example, with time-sliding reference window for studying the tissue relaxation after a perturbation. Figure 6 presents examples of the correlation recovery process. One is observed using a silicone phantom and another is obtained *in vivo* in the mouse ear. The plots show the correlation restoration, characterizing local recovery of the material shape, because the influence of translational displacement is compensated. In these experiments, no special devices for producing perturbations were used. The initial perturbation was produced by pressing on the OCT probe fixed in a clamp and attached to the studied tissue region. The clamping system had certain flexibility so that this could produce displacements on the order of 10–100 μm . After applying the additional pressure, the probe was released to study the subsequent relaxation. The value

of the initial displacement was not very critical for the observed relaxation rate, similar to previously published experiments [41]. The sliding-time correlation between adjacent B-scans was calculated for the subset windows 7×7 pixels and then the resulting field was averaged over the signal area. The red (noisy) curve in Figure 6 is the so-found correlation coefficient as a function of the current frame number (the black curve is its exponential fit).

The presented plots merely demonstrate the possibility of using the CS approach for studying relaxation processes in soft tissues. Obviously, for more accurate measurements, the frame rate should be significantly increased. As mentioned in [41], ample understanding of the physical origin of the observed relaxation requires creation of rather sophisticated models. However, even obtaining comparative (relative) maps showing the distribution of local relaxation rates over the OCT image area may be of interest in itself for distinguishing normal and pathological tissues.

Further, combining the CS and the optical palpation approaches may prove interesting. The latter is based on a

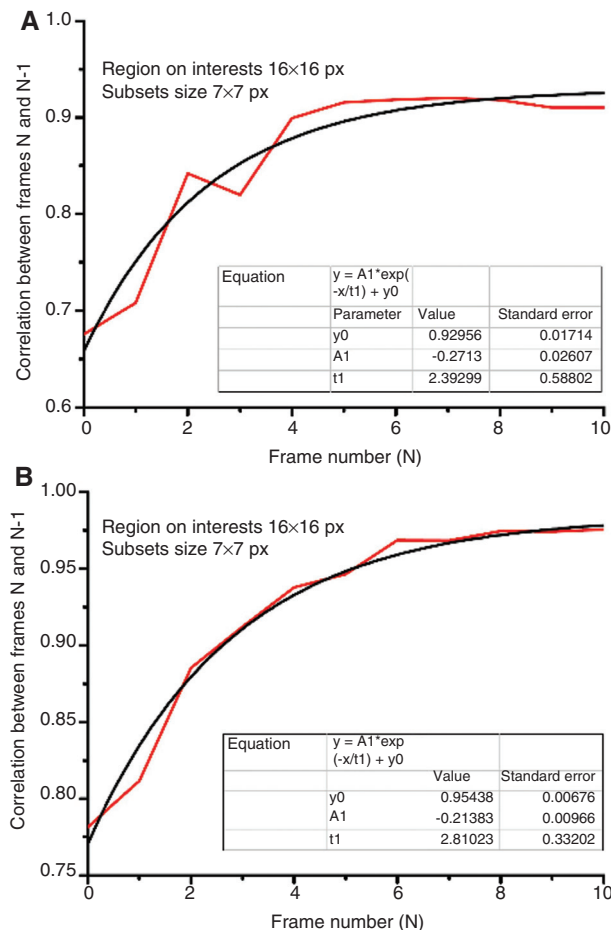


Figure 6 Relaxation process observed in the silicone phantom (A) and *in vivo* a mouse ear (B). Region of interest acts as search area of the subsets translational displacements. The frame rate is 10 fps.

controllable translucent soft layer for visualizing strains due to stiffer tissue inclusions located beneath the layer, even at a depth that cannot be directly visualized by OCT [43]. Since

the CS approach (after properly performed compensation of translational displacements) provides the information about the spatial distribution of local strains, the inhomogeneous strains in the translucent sensor layer can readily be visualized as necessary for the palpation idea. In fact, the softer silicone layer shown in Figure 3 already acts as a reference layer, demonstrating stronger decorrelation compared with the underlying stiffer layer, although Figure 3 still does not demonstrate inhomogeneity in the lateral direction for the contacting horizontal homogeneous layers.

In Figure 7 another example obtained for the two materials similar to those used in Figure 3 is shown. The difference compared to Figure 3 is that now a stiffer plastic inclusion with a near-cylinder cross-sectional shape was embedded between the contacting layers. This “sandwich” structure was put on a rigid plastic plate and was slightly pressed from above by the OCT probe during acquisition of a series of B-scans. Then those scans were cross-correlated with sub-pixel compensation of decorrelation due to translational motions. The residual decorrelation characterizes the values of the local strains. The structural image in Figure 7A allows one to distinguish the boundaries between the silicone layers and the stiffer cylindrical inclusion, although the brightness distribution within the upper uniform layer is rather uniform and does not report on the inhomogeneity of local strains. In contrast, the CS map obtained by cross-correlating sequentially obtained images shown in Figure 7B clearly shows that the upper silicone layer (seen as very uniform in the structural image) actually experiences rather inhomogeneous straining. The zones of stress and strain concentration to the right and to the left from the inclusion are clearly seen via strongly reduced correlation, whereas the area of the stiffer inclusion and the stiffer bottom silicone

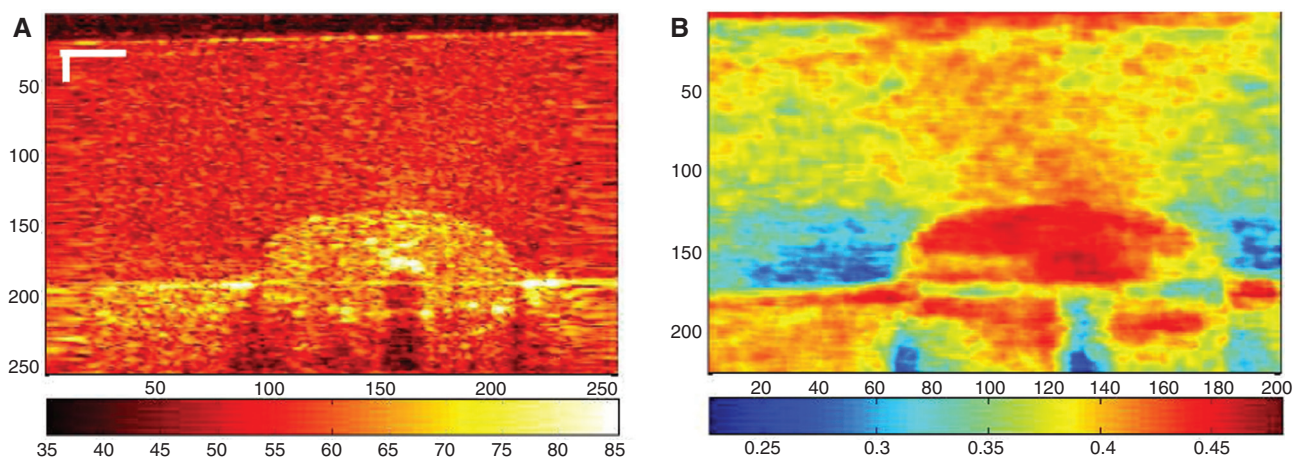


Figure 7 (A) Structural image and (B) the corresponding correlation-stability map for a “sandwich” structure consisting of two silicone layers similar to those used for plotting Figure 3 with additionally embedded stiffer inclusion between the layers. Color-bar under (A) is the logarithm of the intensity and under (B) is ZMNCC. Units of the axis are pixels.

layer clearly demonstrate higher correlation and, correspondingly, smaller strain level. Two small decorrelated regions near the bottom correspond to the dark spots in the structural image where the signal was too low. It is interesting to mention that the upper compliant layer also experiences rather inhomogeneous deformation. The zone of higher correlation in the upper part of the CS map corresponds to the region where the strains are smaller because the silicone is stuck to the rigid surface of the OCT probe (the effect of apparent increased Young's modulus, as discussed in section 2.2). Similarly, in the central part of Figure 7B the stiff insert the local strains are also reduced. This example indicates interesting prospects for combining the CS method of visualizing the local strains with the idea of optical palpation using a translucent compliant layer as a biomechanical sensor.

3 Conclusion

Various OCE techniques demonstrate impressive progress over the last 15 years. However, the approaches proposed for elastographic mapping in OCT still lack the robustness necessary for transferring these methods to real clinical applications. Many OCE-related studies are focused on implementing the basic idea first formulated in [4], according to which the distribution of local strains in the tissue should be determined using the error-prone procedure of differentiation of the initially reconstructed displacement field. Although different methods have been proposed for reconstruction of the displacements (including various modifications of correlational speckle tracking and phase techniques), they all have the same common difficulty related to reconstruction of local strains. In this paper, some alternative approaches proposed for obtaining the elastographic information avoiding the necessity of the differentiation procedures have been discussed. Among such “unconventional” techniques, the recently proposed methods based on relaxation processes [41], the “optical palpation” approach [43], and the CS technique for characterizing local strains [34, 44] were briefly considered. In addition, some possibilities for combining the above-mentioned approaches that can be used for development of new elastographic techniques in OCT were also discussed. It is expected that such “unconventional” methods should prove sufficiently robust to develop practical OCE techniques in the near future.

Acknowledgments: This work is partially supported by the Russian Foundation for Basic Research (grant No. 13-02-00627 and 13-02-97131). L.A. Matveev acknowledges

support of grant No. MK-4826.2013.2 of the President of the Russian Federation. The authors also acknowledge the OCT Lab of the Nizhny Novgorod State Medical Academy (NNSMA) (under Russian Federation Government contract No. 14.B25.31.0015) for organizing and financial supports of the experiments provided in sections 2.4 and 2.5 and the MedLab of the Nizhny Novgorod State University (under Russian Federation Government contract No. 11.G34.31.0066 and Russian Ministry of Education and Science contract No. 02.B.49.21.0003) for partial support of SD-OCE system development.

Authors are grateful to Marina Shirmanova, Marina Sirotkina, Maria Karabut, Tatiana Pryanikova, Vadim Elagin and Anton Pavlikov (all from NNSMA, Nizhny Novgorod, Russia) for their help during the experiments with the mice. Authors also are grateful to Prof. Kirill Larin (University of Houston, USA), Prof. David Sampson (University of Western Australia, Australia) and the co-authors of the works [41, 42] and [43] for reprint permissions and for providing materials for this review.

Conflict of interest statement: The authors declare that there is no conflict of interest with any financial organization regarding the material discussed in the manuscript.

References

- [1] Huang S, Ingber DE. Cell tension, matrix mechanics, and cancer development. *Cancer Cell* 2005;8(3):175–6.
- [2] Sarvazyan A, Hall TJ, Urban MW, Fatemi M, Aglyamov SR, Garra BS. An overview of elastography – An emerging branch of medical imaging. *Curr Med Imaging Rev* 2011;7(4):255–82.
- [3] Parker KJ, Dooley MM, Rubens DJ. Imaging the elastic properties of tissue: the 20 year perspective. *Phys Med Biol* 2011;56(1):R1–R29.
- [4] Schmitt J. OCT elastography: imaging microscopic deformation and strain of tissue. *Opt Express* 1998;3(6):199–211.
- [5] Rogowska J, Patel NA, Fujimoto JG, Brezinski ME. Optical coherence tomographic elastography technique for measuring deformation and strain of atherosclerotic tissues. *Heart* 2004;90(5):556–62.
- [6] Rogowska J, Patel N, Plummer S, Brezinski ME. Quantitative optical coherence tomographic elastography: method for assessing arterial mechanical properties. *Br J Radiol* 2006;79(945):707–11.
- [7] Khalil AS, Chan RC, Chau AH, Bouma BE, Mofrad MR. Tissue elasticity estimation with optical coherence elastography: toward mechanical characterization of in vivo soft tissue. *Ann Biomed Eng* 2005;33(11):1631–9.
- [8] Wang RK, Kirkpatrick S, Hinds M. Phase-sensitive optical coherence elastography for mapping tissue microstrains in real time. *Appl Phys Lett* 2007;90(16):164105.
- [9] Kennedy BF, Hillman TR, McLaughlin RA, Quirk BC, Sampson DD. In vivo dynamic optical coherence elastography using a ring actuator. *Opt Express* 2009;17(24):21762–72.

- [10] Kennedy BF, Liang X, Adie SG, Gerstmann DK, Quirk BC, Boppart SA, Sampson DD. In vivo three-dimensional optical coherence elastography. *Opt Express* 2011;19(7):6623–34.
- [11] Wang S, Li J, Manapuram RK, Menodiado FM, Ingram DR, Twa MD, Lazar AJ, Lev DC, Pollock RE, Larin KV. Noncontact measurement of elasticity for the detection of soft-tissue tumors using phase-sensitive optical coherence tomography combined with a focused air-puff system. *Opt Lett* 2012;37(24):5184–6.
- [12] van Soest G, Mastik F, de Jong N, van der Steen AF. Robust intravascular optical coherence elastography by line correlations. *Phys Med Biol* 2007;52(9):2445–58.
- [13] Nahas A, Bauer M, Roux S, Boccara AC. 3D static elastography at the micrometer scale using full field OCT. *Biomed Opt Express* 2013;4(10):2138–49.
- [14] Sun C, Standish B, Vuong B, Wen XY, Yang V. Digital image correlation-based optical coherence elastography. *J Biomed Opt* 2013;18(12):121515.
- [15] Kennedy KM, Ford C, Kennedy BF, Bush MB, Sampson DD. Analysis of mechanical contrast in optical coherence elastography. *J Biomed Opt* 2013;18(12):121508.
- [16] Kennedy KM, McLaughlin RA, Kennedy BF, Tien A, Latham B, Saunders CM, Sampson DD. Needle optical coherence elastography for the measurement of microscale mechanical contrast deep within human breast tissues. *J Biomed Opt* 2013;18(12):121510.
- [17] Nadkarni SK. Optical measurement of arterial mechanical properties: from atherosclerotic plaque initiation to rupture. *J Biomed Opt* 2013;18(12):121507.
- [18] Liang X, Crecea V, Boppart SA. Dynamic optical coherence elastography: a review. *J Innov Opt Health Sci* 2010;3(4):221–3.
- [19] Sun C, Standish B, Yang VX. Optical coherence elastography: current status and future applications. *J Biomed Opt* 2011;16(4):043001.
- [20] Kennedy BF, Kennedy KM, Sampson DD. A review of optical coherence elastography: fundamentals, techniques and prospects. *IEEE J Sel Topics Quantum Electron* 2014;20(2):1–17.
- [21] Razani M, Mariampillai A, Sun C, Luk TW, Yang VX, Kolios MC. Feasibility of optical coherence elastography measurements of shear wave propagation in homogeneous tissue equivalent phantoms. *Biomed Opt Express* 2012;3(5):972–80.
- [22] Manapuram RK, Aglyamov SR, Monediado FM, Mashiatulla M, Li J, Emelianov SY, Larin KV. In vivo estimation of elastic wave parameters using phase-stabilized swept source optical coherence elastography. *J Biomed Opt* 2012;17(10):100501.
- [23] Li J, Wang S, Manapuram RK, Singh M, Menodiado FM, Aglyamov S, Emelianov S, Twa MD, Larin KV. Dynamic optical coherence tomography measurements of elastic wave propagation in tissue-mimicking phantoms and mouse cornea in vivo. *J Biomed Opt* 2013;18(12):121503.
- [24] Song S, Huang Z, Nguyen TM, Wong EY, Arnal B, O'Donnell M, Wang RK. Shear modulus imaging by direct visualization of propagating shear waves with phase-sensitive optical coherence tomography. *J Biomed Opt* 2013;18(12):121509.
- [25] Nahas A, Tanter M, Nguyen TM, Chassot JM, Fink M, Claude Boccara A. From supersonic shear wave imaging to full-field optical coherence shear wave elastography. *J Biomed Opt* 2013;18(12):121514.
- [26] Nguyen TM, Song S, Arnal B, Wong EY, Huang Z, Wang RK, O'Donnell M. Shear wave pulse compression for dynamic elastography using phase-sensitive optical coherence tomography. *J Biomed Opt* 2014;19(1):16013.
- [27] Razani M, Luk TW, Mariampillai A, Siegler P, Kiehl TR, Kolios MC, Yang VX. Optical coherence tomography detection of shear wave propagation in inhomogeneous tissue equivalent phantoms and ex-vivo carotid artery samples. *Biomed Opt Express* 2014;5(3):895–906.
- [28] Wang S, Larin KV. Shear wave imaging optical coherence tomography (SWI-OCT) for ocular tissue biomechanics. *Opt Lett* 2014;39(1):41–4.
- [29] Wang S, Lopez AL, Morikawa Y, Tao G, Li J, Larina I, Martin JF, Larin KV. Noncontact quantitative biomechanical characterization of cardiac muscle using shear wave imaging optical coherence tomography. *Biomed Opt Express* 2014;5(7):1980–92.
- [30] Kato Y, Wada Y, Mizuno Y, Nakamura K. Measurement of elastic wave propagation velocity near tissue surface by optical coherence tomography and laser Doppler velocimetry. *Jpn J Appl Phys* 2014;53(7S):07KF05.
- [31] Song S, Huang Z, Wang RK. Tracking mechanical wave propagation within tissue using phase-sensitive optical coherence tomography: Motion artifact and its compensation. *J Biomed Opt* 2013;18(12):121505.
- [32] Yun SH, Tearney G, de Boer J, Bouma B. Motion artifacts in optical coherence tomography with frequency-domain ranging. *Opt Express* 2004;12(13):2977–98.
- [33] O'Hara KE, Schmoll T, Vass C, Leitgeb RA. Measuring pulse-induced natural relative motions within human ocular tissue in vivo using phase-sensitive optical coherence tomography. *J Biomed Opt* 2013;18(12):121506.
- [34] Zaitsev VY, Matveev LA, Matveyev AL, Gelikonov GV, Gelikonov VM. Elastographic mapping in optical coherence tomography using an unconventional approach based on correlation stability. *J Biomed Opt* 2014;19(2):21107.
- [35] Fu J, Pierron F, Ruiz PD. Elastic stiffness characterization using three-dimensional full-field deformation obtained with optical coherence tomography and digital volume correlation. *J Biomed Opt* 2013;18(12):121512.
- [36] Kennedy BF, Hillman TR, Curatolo A, Sampson DD. Speckle reduction in optical coherence tomography by strain compounding. *Opt Lett* 2010;35(14):2445–7.
- [37] Kennedy BF, Curatolo A, Hillman TR, Saunders CM, Sampson DD. Speckle reduction in optical coherence tomography images using tissue viscoelasticity. *J Biomed Opt* 2011;16(2):020506.
- [38] Curatolo A, Kennedy BF, Sampson DD, Hillman TR. Speckle in optical coherence tomography. In: Wang RK, Tuchin VV, editors. *Advanced biophotonics: tissue optical sectioning*. Boca Raton: Taylor & Francis; 2014, p. 211–78.
- [39] Kennedy BF, Koh SH, McLaughlin RA, Kennedy KM, Munro PR, Sampson DD. Strain estimation in phase-sensitive optical coherence elastography. *Biomed Opt Express* 2012;3(8):1865–79.
- [40] Zaitsev VY, Gelikonov VM, Matveev LA, Gelikonov GV, Matveyev AL, Shilyagin PA, Vitkin IA. Recent trends in multi-modal optical coherence tomography. I. Polarization-sensitive OCT and conventional approaches to OCT elastography. *Radio-phys Quantum El* 2014;57(1):52–66.
- [41] Li J, Wang S, Singh M, Aglyamov S, Emelianov S, Twa MD, Larin KV. Air-pulse OCE for assessment of age-related changes in mouse cornea in vivo. *Laser Phys Lett* 2014;11(6):065601.

- [42] Wang S, Larin KV, Li J, Vantipalli S, Manapuram RK, Aglyamov S, Emelianov S, Twa MD. A focused air-pulse system for optical-coherence-tomography-based measurements of tissue elasticity. *Laser Phys Lett* 2013;10(7):075605.
- [43] Kennedy KM, Es'haghian S, Chin L, McLaughlin RA, Sampson DD, Kennedy BF. Optical palpation: optical coherence tomography-based tactile imaging using a compliant sensor. *Opt Lett* 2014;39(10):3014–7.
- [44] Zaitsev VY, Matveev LA, Gelikonov GV, Matveyev AL, Gelikonov VM. A correlation-stability approach to elasticity mapping in optical coherence tomography. *Laser Phys Lett* 2013;10(6): 065601.
- [45] Zaitsev VY, Vitkin IA, Matveev LA, Gelikonov VM, Matveyev AL, Gelikonov GV. Recent trends in multimodal optical coherence tomography. II. The correlation-stability approach in OCT elastography and methods for visualization of microcirculation. *Radiophys Quantum El* 2014;57(3):231–50.
- [46] Matveev LA, Zaitsev VY, Matveyev AL, Gelikonov GV, Gelikonov VM. Correlation-stability approach in optical microelastography of tissues. *Proc SPIE* 2013;8699:869904.
- [47] Zaitsev VY, Matveev LA, Matveyev AL, Gelikonov GV, Gelikonov VM. Correlation-stability elastography in OCT: algorithm and in vivo demonstrations. *Proc SPIE* 2013;8802:880208.
- [48] Enfield J, Jonathan E, Leahy M. In vivo imaging of the microcirculation of the volar forearm using correlation mapping optical coherence tomography (cmOCT). *Biomed Opt Express* 2011;2(5):1184–93.
- [49] Jonathan E, Enfield J, Leahy MJ. Correlation mapping method for generating microcirculation morphology from optical coherence tomography (OCT) intensity images. *J Biophotonics* 2011;4(9):583–7.
- [50] Subhash HM, Leahy MJ. Microcirculation imaging based on full-range high-speed spectral domain correlation mapping optical coherence tomography. *J Biomed Opt* 2014;19(2):21103.
- [51] Choi WJ, Reif R, Yousefi S, Wang RK. Improved microcirculation imaging of human skin in vivo using optical microangiography with a correlation mapping mask. *J Biomed Opt* 2014;19(3):36010.
- [52] Zaitsev VY, Matveev LA, Matveyev AL, Gelikonov GV, Gelikonov VM. Towards free-hand implementation of OCT elastography: displacement-based approaches versus correlation-stability ones. *Proc SPIE* 2014;9129:91290J.
- [53] Matveev LA, Zaitsev VY, Matveyev AL, Gelikonov GV, Gelikonov VM. Combining the correlation-stability approach to OCT elastography with the speckle-variance evaluation for quantifying the stiffness differences. *Proc SPIE* 2014;9129:91290I.
- [54] Matveev LA, Zaitsev VY, Matveyev AL, Gelikonov GV, Gelikonov VM. To the problem of stiffness-contrast quantification in the correlation-stability approach to OCT elastography. *Proc SPIE* 2014;9031:903102.
- [55] Mariampillai A, Standish BA, Moriyama EH, Khurana M, Munce NR, Leung MK, Jiang J, Cable A, Wilson BC, Vitkin IA, Yang VX. Speckle variance detection of microvasculature using swept-source optical coherence tomography. *Opt Lett* 2008;33(13):1530–2.
- [56] Mariampillai A, Leung MK, Jarvi M, Standish BA, Lee K, Wilson BC, Vitkin A, Yang VX. Optimized speckle variance OCT imaging of microvasculature. *Opt Lett* 2010;35(8):1257–9.
- [57] Conroy L, DaCosta RS, Vitkin IA. Quantifying tissue microvasculature with speckle variance optical coherence tomography. *Opt Lett* 2012;37(15):3180–2.
- [58] Lee KK, Mariampillai A, Yu JX, Cadotte DW, Wilson BC, Standish BA, Yang VX. Real-time speckle variance swept-source optical coherence tomography using a graphics processing unit. *Biomed Opt Express* 2012;3(7):1557–64.
- [59] Davoudi B, Morrison M, Bizheva K, Yang VX, Dinniwel R, Levin W, Vitkin IA. Optical coherence tomography platform for microvascular imaging and quantification: initial experience in late oral radiation toxicity patients. *J Biomed Opt* 2013;18(7):76008.
- [60] Sudheendran N, Syed SH, Dickinson ME, Larina IV, Larin KV. Speckle variance OCT imaging of the vasculature in live mammalian embryos. *Laser Phys Lett* 2011;8(3):247–52.
- [61] Zaitsev VY, Matveev LA, Matveyev AL, Gelikonov GV, Gelikonov VM. A model for simulating speckle-pattern evolution based on close to reality procedures used in spectral-domain OCT. *Laser Phys Lett* 2014;11(10):105601.